Energy Advances

ROYAL SOCIETY OF CHEMISTRY

PAPER

View Article Online
View Journal | View Issue

Cite this: *Energy Adv.*, 2025, 4, 1500

Analysis of short-circuit current suppression mediated by strategically optimized buffer layer thickness in heterojunction solar cells

Muhammad Umar Salman and Shahid Atiq *

The ever-growing global energy crisis and alarming environmental degradation have intensified the search for sustainable energy alternatives, with solar technology standing at the forefront of this revolution. Among cutting-edge photovoltaic (PV) advancements, heterojunction lead-free perovskite solar cells offer remarkable efficiency and environmental compatibility. This study presents a novel TiO_2/SnS/$BiFeO_3$/spiro-OMeTAD configuration, analysed through COMSOL simulations in 1D to optimize performance. The results demonstrate a maximum efficiency of 23.59% at 1×10^{19} cm^{-3} donor–acceptor (DA) density, confirming the potential of this structure for high-performance applications. Furthermore, the fill factor peaks at 82.94% near 150 nm electron transport thickness, highlighting enhanced charge collection. The open-circuit voltage reaches a maximum of 1.057 V at an SnS layer thickness of 10 nm and decreases with further thickness increase, attributed to the impact on energy band alignment. The short-circuit current is suppressed as the SnS layer's thickness increases, attributed to the impact on the layer's resistance. Conversely, the short-circuit current density attained a peak of 35.330 mA cm^{-2} at a DA density of 1×10^{16} cm^{-3}, due to improved charge carrier concentration at lower densities. These findings establish the feasibility of this heterojunction solar cell structure, providing a strong foundation for future experimental validation and optimization. This research paves the way for the development of next-generation, high-efficiency, and lead-free PV devices, promoting sustainable energy solutions.

Received 4th October 2025,
Accepted 20th October 2025

DOI: 10.1039/d5ya00290g

rsc.li/energy-advances

1. Introduction

The rapid rise in global energy consumption, which surpassed 14.1 gigatons (GT) in 2021, has intensified concerns over resource depletion and environmental sustainability.[1] Fossil fuels remain the dominant source, supplying over 80% of total energy, but their excessive use has led to massive CO_2 emissions, reaching 35.8 GT globally in 2023, along with other harmful gases like methane (CH_4), sulfur oxides (SO_x), and nitrogen oxides (NO_x), further exacerbating environmental issues.[2–4] Global energy demand is expected to surpass 25 000 tera watt (TW) by 2030, making the transition to renewables essential, and solar photovoltaics (PVs) have emerged as a key solution, reaching a global energy capacity of 942 Giga watt (GW) in 2021.[1,5–7] However, conventional single-junction solar cells face fundamental efficiency limits, with the Shockley–Queisser limit capping their maximum efficiency at approximately 33%.[8–13] To address these constraints, heterojunction perovskite solar cells (HPSCs) use multiple absorber layers with complementary bandgaps to enhance light absorption and have achieved 29.8% efficiency.[14,15] This study investigates a HPSC, where tin sulphide (SnS) acts as a buffer layer, bismuth ferrite ($BiFeO_3$) serves as the absorber layer, titanium oxide (TiO_2) functions as the electron transport layer (ETL), and spiro-OMeTAD is used as the hole transport layer (HTL). This configuration is designed to enhance charge carrier dynamics, reduce recombination losses, and achieve higher efficiency than conventional single-junction cells.

The efficiency of HPSCs depends on the precise interaction between its layers, each contributing to charge generation, separation, and transport. The buffer layer, SnS, with a direct bandgap of ~1.3 eV, ensures strong photon absorption and efficient charge carrier generation while remaining an environmentally friendly and earth-abundant material.[16–23] However, effective charge transfer requires an intermediate layer to minimize recombination losses. The absorber layer must exhibit a high absorption coefficient and an optimized bandgap for efficient light harvesting. $BiFeO_3$ (BFO) provides this functionality with its bandgap of around 2.1 eV and ferroelectric properties, which enhance charge separation by generating an internal electric field.[24–27] To facilitate electron extraction and

Centre of Excellence in Solid State Physics, University of the Punjab, Lahore-54590, Pakistan. E-mail: satiq.cssp@pu.edu.pk

transport, a high-mobility material such as TiO_2, commonly used as an ETL, offers a wide bandgap of 3.2 eV that ensures excellent optical transparency and prevents undesired charge recombination.[28–34] On the other hand, charge balance within the device is maintained by an efficient hole-extracting material such as spiro-OMeTAD, which has a bandgap of ~3.0 eV and provides a stable, conductive pathway for hole transport, reducing energy losses and enhancing charge collection.[35,36] The careful selection of these materials, combined with their optimized bandgap alignment, contributes to improved charge extraction, reduced recombination losses, and enhanced overall power conversion efficiency.

For SnS thin films, issues such as poor crystallinity, high density of grain boundaries, and non-stoichiometric growth often lead to enhanced recombination losses and reduced carrier mobility. Similarly, BFO thin films can suffer from oxygen vacancies, secondary phase formation, and instability during post-deposition annealing, which directly affect their ferroelectric and photovoltaic response. Both materials also face long-term stability concerns when exposed to ambient conditions, which can further impact device reliability. To mitigate these challenges, various fabrication approaches have been investigated. For SnS, techniques such as chemical bath deposition, atomic layer deposition, and thermal evaporation have shown promise in producing uniform and highly crystalline layers with controlled stoichiometry. In the case of BFO, sol–gel processing, pulsed laser deposition, and sputtering methods have been widely used to achieve high-quality films with reduced defect density and improved phase purity. In addition, defect passivation strategies, such as interface engineering and incorporation of buffer layers, have been demonstrated to enhance stability and reduce recombination centers.

In this study, COMSOL Multiphysics is employed to model and analyse the charge transport and efficiency performance of the proposed 1D HPSC. The numerical simulations provide valuable insights into band alignment, carrier dynamics, and interfacial charge transfer, enabling the optimization of absorber, buffer, and transport layers to enhance charge collection and minimize recombination losses. This research contributes to the advancement of high-efficiency, lead-free HPSCs, addressing the growing demand for stable and sustainable PV technologies. Future work may focus on further material optimizations, experimental validation, and stability improvements to facilitate the transition from theoretical modelling to practical application in next-generation solar energy systems.

2. Numerical modelling

Numerical modelling is essential in solar cell research, enabling accurate simulation of charge transport, electric field (E) distribution, and recombination processes. COMSOL Multiphysics, employing the finite element method (FEM), effectively models carrier dynamics, electrostatic potential, and recombination mechanisms. SCAPS-1D, based on the drift-diffusion model, is particularly suited for thin-film solar cells offering precise control over band alignment and defect-state modelling. Silvaco ATLAS incorporates quantum mechanical effects, providing detailed insights into tunnelling phenomena, interface states, and recombination behaviour.[37] These tools are instrumental in evaluating key PV parameters: short-circuit current density (J_{sc}), open-circuit voltage (V_{oc}), fill factor (FF), and efficiency, optimizing solar cell performance. Poisson's equation (eqn (1)) governs the distribution of electrostatic potential, establishing a link between the spatial distribution of charge carriers and the E, thereby influencing charge separation and transport:

$$\nabla\cdot(\varepsilon\nabla\psi) = -\rho \quad (1)$$

Here, in eqn (1), ε is the material permittivity, ψ denotes electrostatic potential, and ρ represents the charge density, with ∇ being the vector differential operator describing spatial variation. Carrier transport is governed by the continuity equations (eqn (2) and (3)), which ensure conservation of charge by incorporating the effects of carrier drift, diffusion, generation (G), and recombination (R):

$$\frac{\partial n}{\partial t} = \frac{1}{q}\nabla\cdot J_{\mathrm{n}} + G - R \quad (2)$$

$$\frac{\partial p}{\partial t} = -\frac{1}{q}\nabla\cdot J_{\mathrm{p}} + G - R \quad (3)$$

Here, in eqn (2) and (3), n and p denote electron and hole concentrations, J_{n} and J_{p} are current densities, $\nabla\cdot J_{\mathrm{n}}$ and $\nabla\cdot J_{\mathrm{p}}$ describe current divergence, and q is the elementary charge. The current density equations (eqn (4) and (5)) describe the movement of electrons and holes, considering both drift motion due to the E and diffusion caused by concentration gradients. Drift transport is dominant in high-field regions such as the depletion layer, where carriers are rapidly swept toward their respective electrodes, while diffusion transport occurs in areas with low-field strength, where carriers move randomly due to thermal energy. The mobility (μ_{n}, μ_{p}) of electrons and holes influences the drift component, while the diffusion coefficients (D_{n}, D_{p}) determine how efficiently carriers spread within the semiconductor.

$$J_{\mathrm{n}} = q\mu_{\mathrm{n}}nE + qD_{\mathrm{n}}\nabla_{\mathrm{n}} \quad (4)$$

$$J_{\mathrm{p}} = q\mu_{\mathrm{p}}nE + qD_{\mathrm{p}}\nabla_{\mathrm{p}} \quad (5)$$

Here, in eqn (4) and (5), the elementary charge is denoted by q, while n and p are carrier concentrations, and the gradients of these concentrations are ∇_{n} and ∇_{p}, respectively.[38–45] Recombination is a major loss mechanism that reduces carrier lifetime and efficiency, with Shockley–Read–Hall recombination (R_{SRH}) being the most significant in materials with defects or trap states. This mechanism occurs through mid-gap states, where carriers are captured and re-emitted, leading to non-radiative recombination losses that lower photocurrent generation.[38] R_{SRH} depends on the n and p concentrations, the intrinsic carrier concentration (n_{i}), carrier lifetimes (τ_{n}, τ_{p}), and trap densities for electrons (n_{t}) and holes (p_{t}), influencing

Table 1 Initial parameters of materials used for the respective layers in 1D TiO_2/SnS/BFO/spiro-OMeTAD solar cell simulation

Material properties	TiO_2[46]	SnS[47]	BFO[48]	Spiro-OMeTAD[49]
Thickness (nm)	25	10	10	100
Energy band gap (eV)	3.2	1.3	2.5	3
Relative permittivity	9	13	6	3
Electron affinity (eV)	4.1	4	2.5	1.9
CB effective density of states 'N_C' (cm^{-3})	2×10^{20}	5×10^{19}	5×10^{19}	1×10^{20}
VB effective density of states 'N_V' (cm^{-3})	1×10^{20}	5×10^{19}	5×10^{19}	1×10^{20}
Electron mobility 'μ_n' ($cm^2\ V^{-1}\ s^{-1}$)	20	15	80	2
Hole mobility 'μ_h' ($cm^2\ V^{-1}\ s^{-1}$)	25	100	25	1×10^{-2}
Electron lifetime, SRH, (ns)	1	1000	1000	5
Hole lifetime, SRH, (ns)	1	1000	1000	5

overall device performance, as given in eqn (6):

$$R_{SRH} = \frac{n_p - n_i^2}{\tau_n(p + p_t) + \tau_p(n + n_t)} \quad (6)$$

By solving these fundamental equations using advanced numerical methods in COMSOL Multiphysics, researchers can systematically investigate the impact of material properties, interface defects, and charge transport dynamics on solar cell performance. This enables predictive simulations that guide experimental optimization of materials and fabrication of high-efficiency devices. All the input optimized parameters of each layer for TiO_2/SnS/BFO/spiro-OMeTAD HPSC are tabulated in Table 1.

3. Device simulation and methodology

3.1 Solar absorption and solar spectrum

Fig. 1(a) illustrates the AM1.5 global solar irradiance spectrum, depicting the intensity of sunlight as a function of wavelength and providing a standard representation of the solar radiation that reaches the earth's surface. The spectrum peaks near 500 nm, indicating that the majority of solar energy contribution comes from visible light, while irradiance gradually decreases toward the infrared region (IR). The sharp declines at specific wavelengths are due to atmospheric absorption by gases such as ozone (O_3) in the ultraviolet (UV) range and water vapor (H_2O) and carbon dioxide (CO_2) in the IR.[50] The sharp decline in irradiance beyond 1000 nm indicates that long-wavelength photons possess insufficient energy to excite charge carriers in semiconductors with moderate bandgaps. Conversely, although UV photons carry high energy, their limited availability due to atmospheric filtering reduces their impact on photocurrent generation. This spectral distribution is critical for solar cell design, as the absorber material must have a bandgap well-aligned with the high-intensity portion of the spectrum to ensure maximum efficiency. A large bandgap results in poor absorption of lower-energy photons, while a small bandgap leads to excessive thermalization losses, where surplus photon energy is dissipated as heat rather than converted into electricity. Therefore, understanding the AM1.5 spectrum is essential for selecting suitable absorber materials and device architectures, enabling enhanced photon absorption and charge carrier generation under standard illumination conditions.

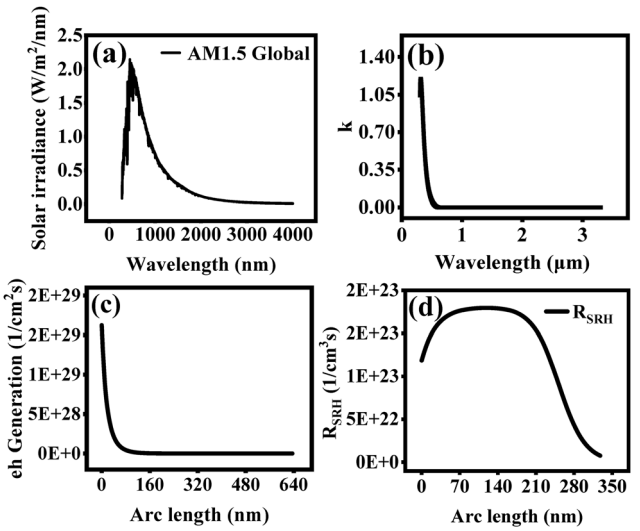

Fig. 1 Optical and electrical characteristics of the device structure: (a) AM1.5 global solar irradiance spectrum, (b) extinction coefficient (k) as a function of wavelength, (c) photogeneration rate distribution along the arc length, and (d) spatial variation of the Shockley–Read–Hall (SRH) recombination rate.

Fig. 1(b) presents the extinction coefficient (k) as a function of wavelength, reflecting the material's ability to attenuate incident photons, which is directly related to the absorption coefficient that defines how deeply light of a specific wavelength can penetrate before being absorbed.[51] A high k value at shorter wavelengths indicates strong absorption in the ultraviolet (UV) and visible regions, which facilitates efficient charge carrier generation near the surface. As the wavelength increases, k decreases sharply, implying that photons in the near-infrared (IR) region are either weakly absorbed or transmitted through the material. This trend suggests that high-energy photons are absorbed within the first few micrometres (μm) of the absorber layer, while low-energy photons can penetrate deeper before being absorbed, or lost in some cases. The steep decline in k at longer wavelengths underscores the difficulty in achieving uniform light absorption across the entire solar spectrum, a key factor in enhancing solar cell efficiency. Interestingly, a lower extinction coefficient in the IR region can be advantageous for HPSCs, as it allows lower-energy photons to transmit through the top cell and be absorbed by an underlying sub-cell with a narrower bandgap. This spectral management enhances photon utilization, thereby contributing significantly to the overall performance of the device.

Fig. 1(c) shows the charge carrier generation rate as a function of arc length within the solar cell, providing insight into the spatial distribution of photogenerated carriers. The highest generation rate occurs at the front surface, where light first interacts with the material, aligning with the high extinction coefficient observed in Fig. 1(b).

As the arc length increases, the generation rate decreases sharply due to the reduced availability of absorbed photons in the deeper layers. This indicates that most electron–hole (e–h) pairs are generated near the illuminated surface, making charge collection efficiency crucial in this region. If the absorber layer is too thin, insufficient photon absorption will limit carrier generation, reducing the photocurrent. Conversely, a thick absorber layer may cause carriers generated in the bulk to recombine before reaching the junction, leading to efficiency losses. The sharp drop-in generation rate with depth suggests that optimizing the absorber thickness is essential to balance absorption and charge transport for efficient solar cell operation.

Fig. 1(d) illustrates the R_{SRH} rate as a function of arc length, highlighting the regions where carrier losses occur due to defect-mediated recombination. Initially, the recombination rate is high near the front surface, likely due to defects or surface traps that act as recombination centres. The recombination rate increases further and peaks at an intermediate depth, indicating a region with a higher density of trap states or bulk defects. Beyond this peak, the recombination rate declines as the number of available charge carriers decreases due to reduced photogeneration in the deeper regions. High recombination near the surface and mid-depth regions reduces carrier lifetime, affecting both the V_{oc} and overall efficiency, thus necessitating effective defect passivation strategies such as surface treatment and doping optimization to suppress recombination losses. Additionally, minimizing defects at critical interfaces, such as the absorber-transport layer junction, can further enhance carrier extraction and improve solar cells.

3.2 Analysis of energy band structure

Fig. 2(a) illustrates the layer-wise design of the solar cell, where light absorption in the BFO layer generates e–h pairs, which are then separated and collected to produce a photocurrent. Electrons move through TiO_2 to the front contact, while holes travel through spiro-OMeTAD to the back contact, driving current flow in the external circuit. Fig. 2(b) illustrates charge carrier transport based on band energies, showing that electrons move from BFO to the SnS layer and then passing through the TiO_2 layer these electrons enter the front contact. Holes migrate through spiro-OMeTAD to the back contact and flow into the external circuit, with arrows indicating the charge movement to ensure efficient separation and extraction, while red crosses denote the forbidden paths for electrons and holes.

Fig. 2(c) shows the energy band diagram of the TiO_2/SnS/BFO/spiro-OMeTAD HPSC along the arc length of the device, with the conduction band edge (E_C) and valence band edge (E_V) exhibiting a step-like variation indicating heterojunction formation at the interfaces. TiO_2 acts as the ETL, facilitating electron movement toward the external circuit, and SnS,

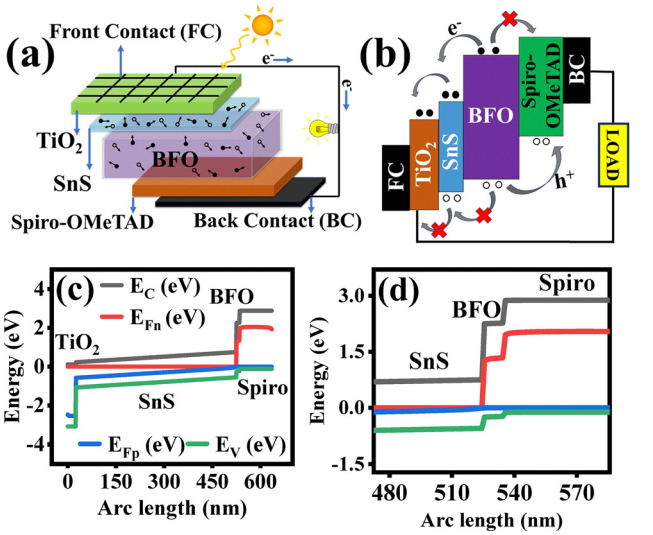

Fig. 2 (a) Schematic representation of the proposed solar cell structure, (b) energy band diagram illustrating the charge transport mechanism under illumination, (c) energy band alignment across the device, indicating conduction band (E_C), valence band (E_V), and Fermi level (E_F) positions, and (d) magnified view of the energy band profile near the BFO/spiro-OMeTAD interface, highlighting carrier extraction dynamics.

positioned in the middle, functions as the buffer layer, where most of the photon absorption and charge generation occur. The BFO layer serves as an absorbing layer, aiding charge separation and transport, while spiro-OMeTAD, the HTL, collects and transfers holes to the electrode, with the electron (E_{F_n}) and hole (E_{F_p}) quasi-Fermi levels showing band bending and efficient charge movement.[52] The band offsets at the junctions ensure proper carrier separation, effectively reducing recombination losses and enhancing V_{oc} for improved device performance.

Fig. 2(d) shows a magnified view of the energy band alignment at the SnS/BFO/spiro-OMeTAD interfaces, where the E_C of SnS is lower than that of BFO, ensuring proper electron confinement and reducing recombination losses. The E_V alignment shows that holes can effectively transfer from SnS to BFO and subsequently to spiro-OMeTAD, supporting efficient hole extraction. The well-separated E_{F_n} and E_{F_p} indicate strong carrier collection and minimal recombination at these interfaces, with the localized band structure playing a critical role in optimizing charge transport and overall device performance.

4. Results and discussion

4.1 Effect of the SnS layer's thickness on HPSC performance

Fig. 3(a) illustrates that as the SnS layer thickness increases, the generation of e–h pairs also increases due to enhanced light absorption, resulting in improved charge carrier production within the solar cell. Fig. 3(b) presents the dependence of current density and applied voltage (J–V) on SnS thickness ranging from 10 nm to 445 nm, showing that increased thickness enhances photon absorption and charge carrier generation.[53,54] Fig. 3(c) shows the power–voltage (P–V) characteristics at various SnS thicknesses, with the highest power

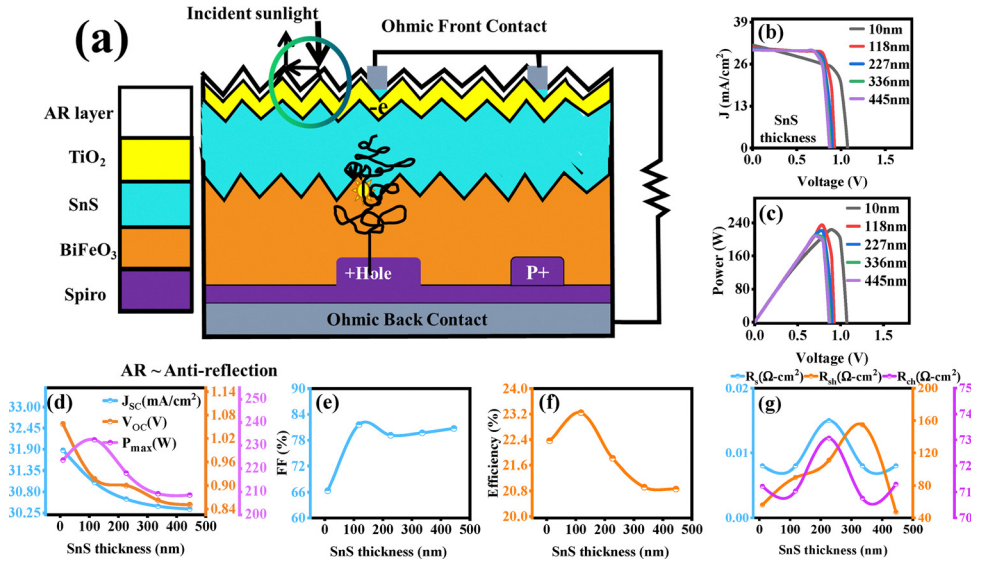

Fig. 3 (a) Cross-sectional schematic of the proposed textured solar cell structure (TiO_2/SnS/$BiFeO_3$/spiro), (b) and (c) J–V and P–V characteristics of the device for varying SnS layer thicknesses, (d)–(f) variation of short-circuit current density (J_{sc}), open-circuit voltage (V_{oc}), and maximum power (P_{max}), fill factor (FF) and efficiency, respectively, and (g) R_s, R_{sh}, and R_{ch} with SnS absorber thickness, demonstrating optimal thickness for maximum performance.

observed at an intermediate thickness, indicating an optimal balance for charge transport and recombination suppression. At very thin or excessively thick SnS layers, power output declines due to either insufficient charge separation or increased recombination losses. Fig. 3(d) reveals that as the buffer layer thickness increases from 15 nm to 150 nm, V_{oc} decreases from ~1.057 V to 0.851 V, and J_{sc} drops from ~31.876 mA cm^{-2} to ~30.349 mA cm^{-2}, likely due to enhanced charge recombination and transport resistance, confirming the suppression of J_{sc} as the SnS layer's thickness increases. Despite this, power maximum (P_{max}) initially rises from 223.623 W at 10 nm to a peak of 232.456 W at 118 nm, then decreases to 208.586 W at 445 nm, confirming that optimal SnS layer thickness is critical for maximizing output.

Fig. 3(e) and (f) shows the variation of FF and efficiency with buffer layer thickness, where both parameters exhibit a fluctuating trend. As the SnS layer thickness increases from 10 nm to 118 nm, FF rises from 66.345% to a peak of 81.627%, and efficiency improves from 22.362% to a maximum of 23.245%, indicating enhanced charge transport and reduced interfacial losses. However, beyond this optimal range, FF drops to 79.713% and efficiency declines to 20.858% at 445 nm, highlighting the impact of excessive thickness on performance. This is due to increased series resistance and recombination losses, which impede charge extraction and lower the overall solar cell performance, reinforcing the importance of optimizing buffer layer thickness for maximum efficiency. The output performance parameters of the TiO_2/SnS/BFO/spiro-OMeTAD HPSC at different buffer layer thicknesses are listed in Table 2.

Table 2 Designed device 1D (TiO_2/SnS/BFO/spiro-OMeTAD) performance parameters with varying SnS thickness

SnS thickness (nm)	J_{sc} (mA cm^{-2})	V_{oc} (V)	P_{max} (W)	FF (%)	Efficiency (%)
10	31.876	1.057	223.623	66.345	22.362
118	31.045	0.917	232.456	81.627	23.245
227	30.611	0.900	218.144	79.155	21.814
336	30.424	0.862	209.174	79.713	20.917
445	30.349	0.851	208.586	80.743	20.858

Fig. 3(g) illustrates the variation of series resistance (R_s), shunt resistance (R_{sh}), and characteristic resistance (R_{ch}) as a function of SnS absorber thickness calculated through Python Software. The maximum R_s (~0.015 Ω cm^2) is observed at a thickness of 227 nm, which can be attributed to the presence of interfacial defects leading to enhanced carrier recombination. As the thickness increases, the density of defects decreases, thereby reducing R_s to 0.008 Ω cm^2 at 336 nm, which corresponds to minimal recombination losses. The R_{sh}, which plays a crucial role in suppressing leakage current and enhancing device performance, reaches its maximum value (~154.7 Ω cm^2) at 336 nm thickness. The R_{ch}, a parameter representing the overall PV response of the device, attains its maximum value (~73.07 Ω cm^2) at 227 nm.[48]

4.2 Effect of ETL thickness on HPSC performance

Fig. 4(a) illustrates that as the ETL thickness increases, the amount of light reaching the underlying layers decreases, which can reduce overall light absorption and impact charge carrier generation in the solar cell. Fig. 4(b) shows the J–V characteristics, while Fig. 4(c) represents the P–V characteristics, showing how J and P output changes with V for different ETL thicknesses. As ETL thickness increases from 25 nm to 150 nm, peak power output decreases due to higher R_s and lower carrier collection efficiency, affecting charge transport and extraction.[55] Fig. 4(d) depicts the dependence of J_{sc}, V_{oc}, and P_{max} on ETL thickness, as ETL thickness increases from 25 nm to 150 nm, J_{sc} decreases from ~31.493 mA cm^{-2} to 7.610 mA cm^{-2}, and V_{oc} reduces from ~0.954 V to ~0.904 V due to increased recombination and transport resistance.

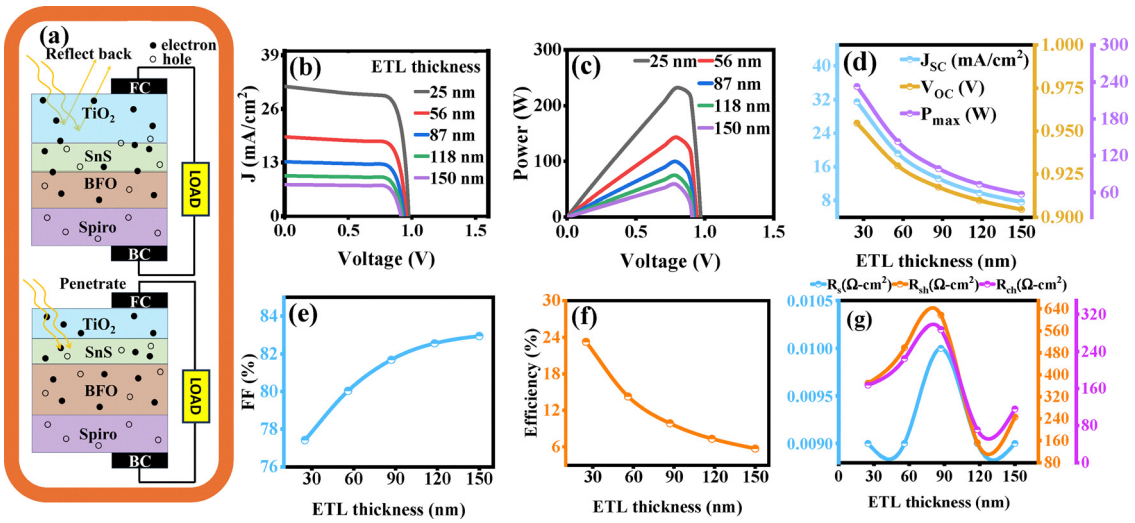

Fig. 4 (a) Schematic of solar cell structure (TiO_2/SnS/$BiFeO_3$/spiro) showing the effect of TiO_2 ETL thickness on light reflection and absorption, (b) and (c) *J*–*V* and *P*–*V* characteristics for different ETL thicknesses, (d) variation of J_{sc}, V_{oc}, and P_{max} with ETL thickness, (e) and (f) influence of ETL thickness on fill factor and efficiency, and (g) R_s, R_{sh}, and R_{ch} with ETL thickness.

Table 3 Designed device 1D (TiO_2/SnS/BFO/spiro-OMeTAD) performance parameters with varying ETL (TiO_2) thickness

TiO_2 thickness (nm)	J_{sc} (mA cm^{-2})	V_{oc} (V)	P_{max} (W)	FF (%)	Efficiency (%)
25	31.493	0.954	232.72	77.41	23.27
56.25	19.196	0.929	142.84	80.03	14.28
87.5	13.172	0.917	98.69	81.68	9.86
118.75	9.761	0.909	73.32	82.56	7.33
150	7.610	0.904	57.09	82.94	5.70

Similarly, P_{max} declines from ~232 W at 25 nm to nearly 57 W at 150 nm, indicating that excessive ETL thickness hinders charge extraction and significantly reduces overall device performance. Fig. 4(e) illustrates that as ETL thickness increases from 25 nm to 150 nm, FF gradually increases from 77.41% at 25 nm to 82.94% at 150 nm. In Fig. 4(f), efficiency decreases gradually from 23.27% at 25 nm to 5.70% at 150 nm, attributed to increased R_s and charge recombination. The output performance parameters of TiO_2/SnS/BFO/spiro-OMeTAD HPSC at different ETL thicknesses are tabulated in Table 3.

Fig. 4(g) presents the correlation between R_s, R_{sh}, and R_{ch} with respect to the ETL layer thickness. A higher R_s (~0.01 Ω cm^2) is recorded at 87 nm, primarily due to the elevated defect density at the ETL/absorber interface. Beyond this thickness, R_s decreases gradually to ~0.009 Ω cm^2, owing to the reduction in interfacial defect states. The maximum R_{sh} (~616 Ω cm^2) is also observed at 87 nm, signifying minimal carrier recombination and suppressed defect-induced pathways. Furthermore, R_{ch} exhibits a peak value of ~287.3 Ω cm^2 at 87 nm thickness; however, with further increase in ETL thickness, R_{ch} declines as recombination losses become more prominent.[56]

4.3 Effect of HTL thickness on HPSC performance

Fig. 5(a) illustrates the role of the HTL in facilitating hole extraction, ensuring efficient charge transport and reducing recombination losses in the solar cell. In Fig. 5(b), the *J*–*V* characteristics with HTL thickness ranging from 100 nm to 150 nm show stable *J* (~31.5 mA cm^{-2}) up to *V* (~0.8 V) then sharply decline. This indicates that charge transport and recombination remain almost unaffected within this range, ensuring efficient hole extraction, with notable performance changes likely occurring only at extreme thickness variation. Fig. 5(c) presents the *P*–*V* characteristics, demonstrating a peak *P* output around 0.8 V for HTL thicknesses between 100 and 150 nm, suggesting stable device performance. The overlapping curves imply that the HTL thickness range has negligible impact on power generation, with only extreme changes potentially influencing resistance, charge transport, and overall efficiency.[57,58]

Fig. 5(d) shows that as HTL thickness increases from 100 nm to 125 nm, V_{oc} remains stable around 0.955 V, slightly increasing to 0.959 V at 137.5 nm due to improved hole transport, before dropping back to 0.955 V at 150 nm, likely due to increased R_s.[48] Minor increases in J_{sc} (31.49 to 31.58 mA cm^{-2}) and P_{max} (232.7 to 233.4 W) suggest improved charge collection at optimized thickness, though the effect is limited. Fig. 5(e) and (f) indicates that FF slightly decreases from 77.39% at 100 nm to 77.03% at 137.5 nm, then recovers to 77.34% at 150 nm, reflecting minor variations in charge transport and recombination. Efficiency gradually increases from 23.272% to 23.348% as HTL thickness increases from 100 nm to 150 nm, indicating improved charge extraction and reduced resistive losses. Overall, these trends confirm that optimized HTL thickness enhances solar cell performance, while excessive thickness may introduce resistance limitations affecting FF stability. The output performance parameters of the TiO_2/SnS/BFO/spiro-OMeTAD HPSC at various ETL thicknesses are displayed in Table 4.

Fig. 5(f) demonstrates the effect of HTL thickness (100–150 nm) on R_s, R_{sh}, and R_{ch}. At 100 nm thickness, R_s reaches

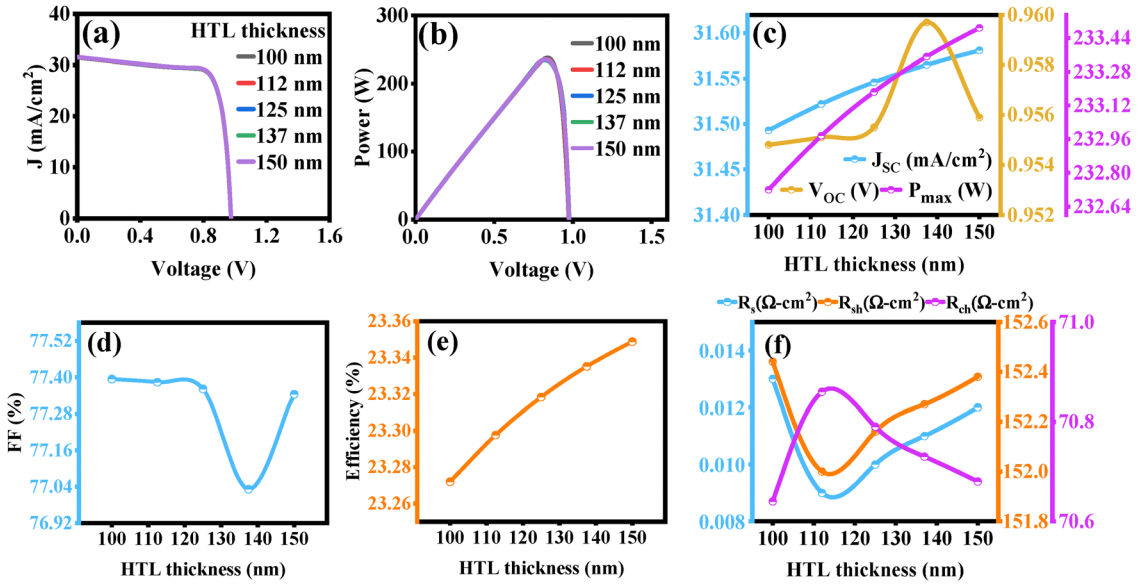

Fig. 5 Effect of HTL thickness variation (100–150 nm) on device (TiO_2/SnS/$BiFeO_3$/spiro) performance parameters: (a) *J–V* characteristics, (b) *P–V* response, (c) variation of J_{sc}, V_{oc}, and P_{max}, (d) and (e) corresponding changes in fill factor and efficiency, and (f) R_s, R_{sh}, and R_{ch} with HTL thickness.

its maximum (~0.013 Ω cm^2), but decreases to ~0.009 Ω cm^2 at 112 nm, indicating reduced recombination and improved charge transport. The maximum R_{sh} (~152.44 Ω cm^2) is observed at 100 nm, which is associated with lower defect density; however, as the HTL thickness increases, R_{sh} diminishes due to enhanced recombination. Similarly, R_{ch} attains its peak (~70.86 Ω cm^2) at 112 nm, after which it slightly decreased, a trend attributed to the increased defect density and recombination losses at higher HTL thicknesses.[59]

4.4 Effect of donor–acceptor densities on HPSC performance

Fig. 6(a) visualizes the distribution of electron and hole concentrations alongside donor and acceptor densities, highlighting the influence of doping levels on charge carrier behaviour within the solar cell structure. In Fig. 6(b), *J–V* characteristics for various donor–acceptor (DA) densities, ranging from 1 × 10^{14} cm^{-3} to 1 × 10^{19} cm^{-3}, show that *J* gradually decreases with increasing *V* for all DA values and drops sharply near 0.8 V. The *P–V* curve in Fig. 6(c) demonstrates that *P* initially rises with *V*, reaching a peak, and then declines sharply. Higher DA densities enhance charge carrier generation and suppress recombination losses, resulting in improved P extraction and better solar cell performance. Fig. 6(d) indicates that J_{sc} initially increases from 30.08 mA cm^{-2} to 35.33 mA cm^{-2}, as DA density rises from 1 × 10^{14} cm^{-3} to 1 × 10^{17} cm^{-3} but subsequently drops to 29.83 mA cm^{-2} at 1 × 10^{19} cm^{-3}, likely due to enhanced recombination at higher doping levels.[60] The V_{oc} decreases from 0.96 V to 0.945 V up to 1 × 10^{16} cm^{-3}, then slightly recovers to ~0.954 V, indicating reduced carrier lifetime effects.[60] P_{max} steadily increases from 135.13 W to 235.90 W, suggesting that increasing DA density improves performance until recombination losses begin to dominate.

Fig. 6(e) presents the variation of FF and efficiency with DA density ranging from 1 × 10^{14} cm^{-3} to 1 × 10^{19} cm^{-3}, showing an increase in FF from 46.60% at 1 × 10^{14} cm^{-3} to 82.83% at 1 × 10^{19} cm^{-3}, while efficiency rises from 13.51% to 23.59%. These enhancements indicate that higher DA densities facilitate better charge collection and reduce recombination, resulting in superior device performance.[61] The output performance parameters of the TiO_2/SnS/BFO/spiro-OMeTAD HPSC at different ETL thicknesses are presented in Table 5.

A comparative analysis of SnS and BFO-based solar cells, incorporating both simulated and experimental data, is summarized in Table 6, highlighting the influence of different ETL and HTL layers on device performance. The Mo/SnS/CdS/i-ZnO/AZO/Al structure demonstrated a low PCE of 4.21%, primarily due to a reduced V_{oc}, which indicated pronounced recombination losses and inefficient charge carrier transport.[62] In contrast, the NiO-based device exhibited an improved PCE of 8.15%, attributed to enhancement in both the FF (65%) and V_{oc}, reflecting superior band alignment and more efficient charge extraction.[47] For the ZnSe/BFO/spiro-OMeTAD configuration (without ITO), a significant improvement was observed, achieving a V_{oc} of 1.96 V and a PCE of 10.73%.[48] Furthermore, employing ZnO as the ETL with a BFO absorber resulted in enhanced device performance, indicating favourable band alignment and reduced recombination pathways.[49] Experimental investigation of SnS-based structures (Mo/SnS/CdS/ZnO) revealed

Table 4 Designed device 1D (TiO_2/SnS/BFO/spiro-OMeTAD) performance parameters with varying HTL (spiro-OMeTAD) thickness

Spiro-OMeTAD thickness (nm)	J_{sc} (mA cm^{-2})	V_{oc} (V)	P_{max} (W)	FF (%)	Efficiency (%)
100	31.493	0.954	232.72	77.39	23.272
112.5	31.522	0.955	232.97	77.38	23.297
125	31.546	0.955	233.18	77.36	23.318
137.5	31.565	0.959	233.35	77.03	23.335
150	31.581	0.955	233.48	77.34	23.348

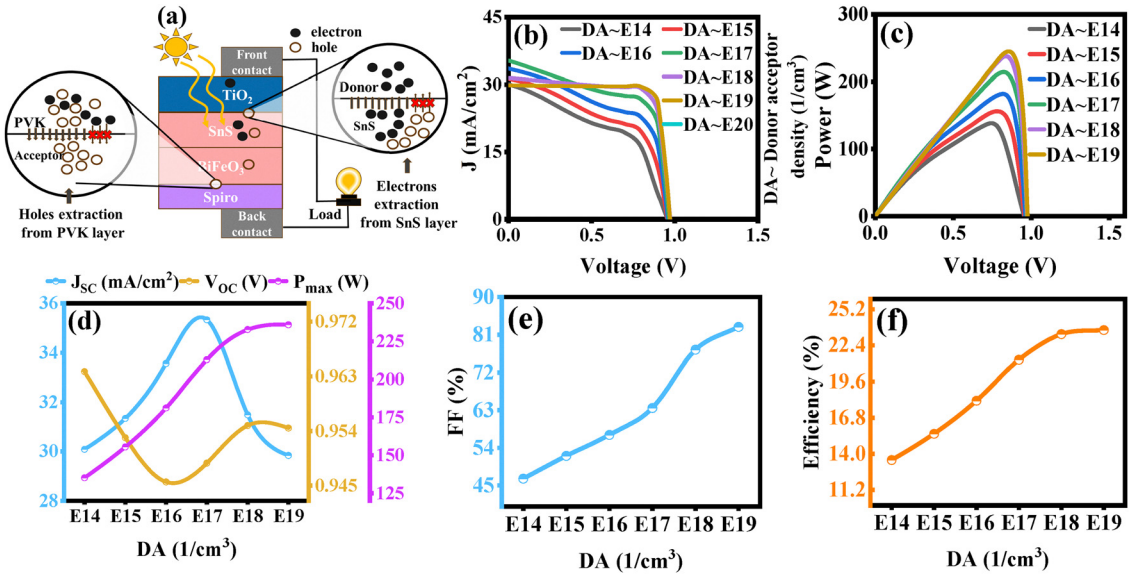

Fig. 6 (a) Schematic representation of the heterojunction solar cell based on the TiO_2/SnS/$BiFeO_3$ (PVK)/spiro configuration with carrier transport mechanisms, (b) and (c) *J*–*V* and *P*–*V* response under varying acceptor densities (DA) in the PVK layer, (d) variation in J_{sc}, V_{oc}, and P_{max}, and (e) and (f) corresponding changes in fill factor and efficiency as a function of DA.

Table 5 Designed device 1D (TiO_2/SnS/BFO/spiro-OMeTAD) performance parameters with varying donor/acceptor (DA) density

DA density (1 cm^{-3})	J_{sc} (mA cm^{-2})	V_{oc} (V)	P_{max} (W)	FF (%)	Efficiency (%)
1×10^{14}	30.080	0.963	135.13	46.60	13.51
1×10^{15}	31.340	0.952	155.48	52.06	15.54
1×10^{16}	33.560	0.945	181.20	57.08	18.12
1×10^{17}	35.330	0.948	212.96	63.52	21.29
1×10^{18}	31.490	0.954	232.72	77.38	23.27
1×10^{19}	29.830	0.954	235.90	82.83	23.59

a limited PCE of 4.22%, arising from a low FF (58%) and V_{oc} (0.34 V), again suggesting high recombination activity.[63] A TiO_2-based architecture yielded a modest improvement in PCE (5.24%) due to a higher FF (68%), consistent with improved band alignment and more effective charge transport.[64] In contrast to these conventional designs, our proposed novel configuration, TiO_2/SnS/BFO/spiro-OMeTAD, demonstrated superior performance, achieving a remarkably high FF (82.83%) and J_{sc} of 29.83 mA cm^{-2}, resulting in a record PCE of 23.59%. The dual absorber system, integrating SnS and BFO, enabled better band alignment and enhanced charge carrier generation, thereby significantly improving overall device efficiency. The incorporation of TiO_2 as the ETL not only facilitated smoother electron extraction with reduced recombination compared to traditional ETLs such as ZnSe and ZnO, but also offered a non-toxic, stable, and environmentally benign alternative. Collectively, the utilization of TiO_2, SnS, and BFO being lead-free and environmentally sustainable positions the proposed architecture as a highly promising candidate for next-generation, eco-friendly photovoltaic devices. All the output numeric values are under the upper theoretical limit as reported by Arturo Morales-Acevedo.[65]

5. Conclusion

This study presents the design and simulation of a TiO_2/SnS/BFO/spiro-OMeTAD solar cell using COMSOL Multiphysics, achieving a peak efficiency of 23.59%. The optimization of SnS (buffer layer) thickness from 10 nm to 445 nm resulted in an open-circuit voltage (V_{oc}) ranging from 1.057 V to 0.91 V, a short-circuit current density (J_{sc}) that was suppressed from 31.876 mA cm^{-2} to 30.349 mA cm^{-2} as the thickness increased,

Table 6 Comparative analysis of the physical parameters of various SnS and BFO-based simulated and experimental device structures for efficient solar cell design

Cell structures	J_{sc} (mA cm^{-2})	V_{oc} (V)	FF %	Efficiency %	Ref.
Mo/SnS/CdS/i-ZnO/AZO/Al (simulation)	19.96	0.34	61.23	4.21	62
NiO/SnS/i/CdS/ZnO/ITO (simulation)	17.00	0.73	65.00	8.15	47
ZnSe/BFO/spiro-OMeTAD (simulation)	8.83	1.96	61.91	10.73	48
ZnO/BFO/spiro-OMeTAD (simulation)	8.99	2.00	65.47	11.87	49
Mo/SnS/CdS/ZnO (experimental)	20.76	0.34	58.00	4.22	63
TiO_2/n-SnS/SnS/Ag/SnS/p-SnS/ITO (experimental)	17.13	0.45	68.00	5.24	64
TiO_2/SnS/BFO/spiro-OMeTAD (simulation)	29.83	0.95	82.83	23.59	This work

and a decrease in power maximum (P_{max}) from 223.623 W and 208.586 W, with the fill factor (FF) reaching 80.743%. Variation in ETL thickness from 25 to 150 nm significantly impacted device performance, with J_{sc} decreasing from 31.493 mA cm^{-2} to 7.610 mA cm^{-2}, V_{oc} slightly declining to 0.904 V, and P_{max} reducing from 232.72 W to 57.09 W. The FF peaked at 82.94% at 150 nm, while efficiency peaked at 23.27% at an ETL thickness of 25 nm before declining. Variation in HTL thickness from 100 nm to 150 nm also influenced efficiency, with V_{oc} between 0.954 V and 0.955 V, J_{sc} ranging from 31.493 mA cm^{-2} to 31.581 mA cm^{-2}, and the P_{max} increasing from 232.72 W to 233.48 W, while the FF is maximum (77.39%) at 25 nm. Further optimization of the donor and acceptor densities resulted in a J_{sc} decrease from 30.08 mA cm^{-2} to 29.83 mA cm^{-2}, a V_{oc} decrease from 0.963 V to 0.954 V, and P_{max} increasing from 135.13 W to 235.90 W, while the FF ranged from 46.60% to 82.83%, resulting in an overall efficiency range of 13.51% to 23.59%. Furthermore, the series resistance (R_s), shunt resistance (R_{sh}), and characteristic resistance (R_{ch}) were calculated using Python software, revealing a maximum R_{sh} of 616 Ω cm^2 at an ETL layer thickness of 87 nm. These results highlight SnS as a highly efficient buffer layer in heterojunction solar cells, demonstrating its ability to outperform many conventional lead-free configurations. Future research should focus on optimizing interfacial properties, enhancing material stability, and exploring alternative transport layers to further improve efficiency and practical applicability.

Conflicts of interest

There are no conflicts to declare.

Data availability

The data will be available on request.

Acknowledgements

The authors would like to acknowledge University of the Punjab, Lahore Annual Research Grant Program for the FY 2024–25.

References

1 O. O. Yolcan, *Innov. Green Dev.*, 2023, **2**(4), 100070.
2 Z. Liu, Z. Deng, S. J. Davis and P. Ciais, *Nat. Rev. Earth Environ.*, 2024, **5**(4), 253–254.
3 X. Wang and L. Yan, *Fuel*, 2022, **314**, 122869.
4 R. Prăvălie, C. Patriche and G. Bandoc, *J. Cleaner Prod.*, 2019, **209**, 692–721.
5 R. K. Yadav, P. S. Pawar, Y. T. Kim, I. Sharma, P. R. Patil, N. Bisht and J. Heo, *Sol. Energy*, 2023, **266**, 112174.
6 V. Ganapavarapu and U. Nanda, *J. Electron. Mater.*, 2025, 1–14.
7 P. K. Dakua, R. K. Dash, A. Laidouci, S. Bhattarai, U. Dudekula, S. Kashyap, V. Agarwal and A. N. Z. Rashed, *J. Electron. Mater.*, 2024, **53**(4), 2015–2025.
8 J. K. W. Ho, H. Yin and S. K. So, *J. Mater. Chem. A*, 2020, **8**(4), 1717–1723.
9 O. D. Miller, E. Yablonovitch and S. R. Kurtz, *IEEE J. Photovolt.*, 2012, **2**(3), 303–311.
10 M. Yamaguchi, F. Dimroth, J. F. Geisz and N. J. Ekins-Daukes, *J. Appl. Phys.*, 2021, **129**(24), 240901.
11 T. T. Ferdous, S. S. Urmi, M. A. K. Khan and M. A. Alim, *Micro Nanostruct.*, 2024, **192**, 207881.
12 M. Cheraghizade, F. Jamali-Sheini and P. Shabani, *Mater. Sci. Semicond. Process.*, 2019, **90**, 120–128.
13 G. Venkateswarlu and U. Nanda, *IEEE Access*, 2025, **13**, 62648–62659.
14 J. Yan, T. J. Savenije, L. Mazzarella and O. Isabella, *Sustainable Energy Fuels*, 2022, **6**(2), 243–266.
15 A. Singh, V. Srivastava, S. Agarwal, P. Lohia, D. K. Dwivedi, A. Umar, A. A. Ibrahim, S. Akbar, S. Baskoutas and P. K. Dakua, *J. Opt.*, 2024, **53**(4), 3695–3707.
16 B. Islam, A. Hosen, T. M. Khan, M. F. Rahman, M. H. Rahman, M. S. Islam and S. R. A. Ahmed, *J. Electron. Mater.*, 2024, **53**(8), 4726–4739.
17 M. R. Arefi-Rad and H. Kafashan, *Ceram. Int.*, 2024, **50**(18), 31826–31844.
18 M. T. Islam, A. Kumar and A. K. Thakur, *J. Electron. Mater.*, 2021, **50**, 3603–3613.
19 S. Pandey, Sadanand, P. K. Singh, P. Lohia and D. K. Dwivedi, *Trans. Electr. Electron. Mater.*, 2021, **22**(6), 893–903.
20 R. K. Yadav, P. S. Pawar, Y. T. Kim, I. Sharma and J. Heo, *J. Mater. Chem. A*, 2024, **12**(6), 3265–3275.
21 R. K. Yadav, N. Bisht, P. R. Patil, H. J. Ki, S. W. Lee, Y. T. Kim, P. S. Pawar, I. Sharma, M. Vishesh and J. Heo, *Curr. Appl. Phys.*, 2024, **68**, 169–179.
22 M. T. Islam and A. K. Thakur, *Phys. Scr.*, 2023, **98**(10), 105950.
23 D. Lim, H. Suh, M. Suryawanshi, G. Y. Song, J. Y. Cho, J. H. Kim and J. Heo, *Adv. Energy Mater.*, 2018, **8**(10), 1702605.
24 E. Djatoubai, M. S. Khan, S. ul Haq, P. Guo and S. Shen, *Appl. Catal., A*, 2022, **643**, 118737.
25 H. A. A. Khan, S. Ullah, G. Rehman, S. Khan and I. Ahmad, *J. Phys. Chem. Solids*, 2021, **148**, 109737.
26 M. Benyoussef, Y. Nassereddine, S. Saitzek, J. F. Blach, M. El Marssi, A. Sayede and M. Jouiad, *Fuel*, 2025, **381**, 133579.
27 C. Saravanan, P. B. Bhargav, N. Venkateswaran, N. Ahmed, K. Aravinth and C. Balaji, *Eur. Phys. J.: Appl. Phys.*, 2023, **98**, 54.
28 Y. E. Tasisa, T. K. Sarma, R. Krishnaraj and S. Sarma, *Results Chem.*, 2024, **11**, 101850.
29 I. Apostolova, A. Apostolov and J. Wesselinowa, *Nanomaterials*, 2022, **13**(1), 145.
30 P. S. Basavarajappa, S. B. Patil, N. Ganganagappa, K. R. Reddy, A. V. Raghu and C. V. Reddy, *Int. J. Hydrogen Energy*, 2020, **45**(13), 7764–7778.
31 F. Irfan, M. U. Tanveer, M. A. Moiz, S. W. Husain and M. Ramzan, *Eur. Phys. J. B*, 2022, **95**(11), 184.
32 X. Kang, S. Liu, Z. Dai, Y. He, X. Song and Z. Tan, *Catalysts*, 2019, **9**(2), 191.

33 A. K. Chakraborty, S. Ganguli and M. A. Sabur, *J. Water Process Eng.*, 2023, **55**, 104183.
34 M. B. Kanoun, F. Ahmed, C. Awada, C. Jonin and P. F. Brevet, *Int. J. Hydrogen Energy*, 2024, **51**, 907–913.
35 P. Sahoo, C. Tiwari, S. Kukreti and A. Dixit, *J. Alloys Compd.*, 2024, **981**, 173599.
36 A. Javed, M. F. Nasir, I. Qasim, Y. M. Alanazi and M. T. Khan, *Int. J. Electrochem. Sci.*, 2024, **19**(8), 100641.
37 G. P. S. Prashanthi and U. Nanda, *IEEE Access*, 2024, **12**, 114995–115005.
38 G. Pindolia, S. M. Shinde and P. K. Jha, *Sol. Energy*, 2022, **236**, 802–821.
39 R. K. Yadav, P. S. Pawar, R. Nandi, K. E. Neerugatti, Y. T. Kim, J. Y. Cho and J. Heo, *Sol. Energy Mater. Sol. Cells*, 2022, **244**, 111835.
40 N. El Ouarie, J. El Hamdaoui, G. S. Sahoo, K. G. Rodriguez-Osorio, M. Courel, M. Zazoui, L. M. Pérez, D. Laroze and E. Feddi, *Sol. Energy*, 2023, **263**, 111929.
41 M. Ayad, M. Fathi and A. Mellit, *Optik*, 2021, **233**, 166619.
42 O. Ahmad, A. Rashid, M. W. Ahmed, M. F. Nasir and I. Qasim, *Opt. Mater.*, 2021, **117**, 111105.
43 M. Al-Hattab, M. Khenfouch, O. Bajjou, Y. Chrafih and K. Rahmani, *Sol. Energy*, 2021, **227**, 13–22.
44 M. A. Nalianya, C. Awino, H. Barasa, V. Odari, F. Gaitho, B. Omogo and M. Mageto, *Optik*, 2021, **248**, 168060.
45 A. N. Abena, A. T. Ngoupo, F. A. Abega and J. M. B. Ndjaka, *Chin. J. Phys.*, 2022, **76**, 94–109.
46 D. K. Jarwal, A. K. Mishra, A. Kumar, S. Ratan, A. P. Singh, C. Kumar, B. Mukherjee and S. Jit, *Superlattices Microstruct.*, 2020, **140**, 106463.
47 A. Kumar, R. T. Prabu and A. Das, *Opt. Quantum Electron.*, 2022, **54**(8), 521.
48 M. M. Mudassar, M. Arshad, M. U. Salman, A. Mahmood, W. Al-Masry, M. Asim and S. Atiq, *RSC Adv.*, 2025, **15**(40), 33830–33843.
49 M. U. Salman, M. Bilal, Y. K. Karmani, U. Ali, S. M. Ramay, M. Younis and S. Atiq, *J. Mater. Chem. A*, 2025, **13**(20), 15057–15066.
50 M. Sheikholeslami and Z. Khalili, *Sustainable Cities Soc.*, 2024, **101**, 105139.
51 J. Guerroum, M. Al-Hattab, Y. Chrafih, L. H. Moudou, K. Rahmani, Y. Lachtioui and O. Bajjou, *Sol. Energy*, 2023, **266**, 112194.
52 S. Ahmmed, A. Aktar, J. Hossain and A. B. M. Ismail, *Sol. Energy*, 2020, **207**, 693–702.
53 E. Raza, Z. Ahmad, F. Aziz, M. Asif, A. Ahmed, K. Riaz, J. Bhadra and N. J. Al-Thani, *Sol. Energy*, 2021, **225**, 842–850.
54 A. Mortadi, E. El Hafidi, M. Monkade and R. El Moznine, *Mater. Sci. Energy Technol.*, 2024, **7**, 158–165.
55 M. S. Pawar, A. Raj, A. K. Singh, V. Tuli, A. Anshul and M. Kumar, *Mater. Today: Proc.*, 2022, **67**, 713–718.
56 R. Malani, T. Pansuriya and V. Kheraj, *Opt. Mater.*, 2022, **133**, 112910.
57 O. Saidani, A. Yousfi, D. P. Samajdar, X. Xu, T. B. Zemene, S. Bhattarai, M. K. Hossain and G. S. Sahoo, *Sol. Energy Mater. Sol. Cells*, 2024, **277**, 113122.
58 A. A. Abdelkadir, E. Oublal, M. Sahal and A. Gibaud, *Results Opt.*, 2022, **8**, 100257.
59 B. K. Ravidas, A. R. Kumar, A. Praveen, S. K. Agnihotri, S. Bhattarai, R. Pandey, J. Madan, S. Singh, M. K. Hossain, M. K. Roy and D. P. Samajdar, *J. Phys. Chem. Solids*, 2025, **196**, 112325.
60 R. Ranjan, N. Anand, M. N. Tripathi, N. Srivastava, A. K. Sharma, M. Yoshimura, L. Chang and R. N. Tiwari, *Sci. Rep.*, 2023, **13**(1), 18411.
61 M. Mottakin, D. K. Sarkar, V. Selvanathan, M. J. Rashid, K. Sobayel, A. M. Hasan, M. A. Islam, G. Muhammad, Md. Shahiduzzaman and M. Akhtaruzzaman, *Optik*, 2023, **272**, 170232.
62 A. Hosen and S. R. Al Ahmed, *J. Alloys Compd.*, 2022, **909**, 164823.
63 J. Y. Cho, S. Kim, R. Nandi, J. Jang, H. S. Yun, E. Enkhbayar, J. H. Kim, D. K. Lee, C. H. Chung, J. Kim and J. Heo, *J. Mater. Chem. A*, 2020, **8**(39), 20658–20665.
64 T. D. Nguyen, N. M. Hung, V. K. Arepalli, J. Kim, M. Raj and T. T. O. Nguyen, *Surf. Interfaces*, 2021, **25**, 101151.
65 A. Morales-Acevedo, *Sol. Energy*, 2023, **262**, 111774.